Journal of Alloys and Compounds 509 (2011) 6571–6577

Contents lists available at ScienceDirect

Journal of Alloys and Compounds

journal homepage: www.elsevier.com/locate/jallcom

Structural, microstructural and magnetic properties of amorphous/nanocrystalline $Ni_{63}Fe_{13}Mo_4Nb_{20}$ powders prepared by mechanical alloying

L. Karimi [a,*], H. Shokrollahi [b]

[a] Materials Science and Engineering Department, Islamic Azad University of Ahvaz, Ahvaz, Iran
[b] Materials Science and Engineering Department, Shiraz University of Technology, 71555-313, Shiraz, Iran

ARTICLE INFO

Article history:
Received 3 October 2010
Received in revised form 6 March 2011
Accepted 9 March 2011
Available online 17 March 2011

Keywords:
Amorphous materials
Mechanical alloying
Magnetic measurements
X-ray diffraction

ABSTRACT

This paper focuses on the magnetic, structural and microstructural studies of amorphous/nanocrystalline $Ni_{63}Fe_{13}Mo_4Nb_{20}$ powders prepared by mechanical alloying. The ball-milling of Ni, Fe, Mo and Nb powders leads to alloying the element powders, the nanocrystalline and an amorphization matrix with Mo element up to 120 h followed by the strain and thermal-induced nucleation of a single nanocrystalline Ni-based phase from the amorphous matrix at 190 h. The results showed that the saturation magnetization decreases as a result of the electronic interactions between magnetic and non-magnetic elements and finally increases by the partial crystallization of the amorphous matrix. The coercive force increases as the milling time increases and finally decreases due to sub-grains formation.

1. Introduction

Almost all magnetic alloys contain at least one of the iron, cobalt and nickel elements. By alloying these metals, the magnetic substances with different magnetic and electrical properties can be obtained. Ni–Fe-based alloys are commonly used as the magnetic materials exhibiting high permeability, low coercivity, high electrical resistivity and low magnetostriction [1–4]. By alloying the Ni–Fe alloys with ternary elements, such as Mo and changing the real structure from crystallite to the amorphous state, various kinds of magnetic, electrical and structural properties can be achieved [5,6].

The amorphous magnetic alloys can be prepared by mechanical alloying (MA) via solid-state transformations. The process of mechanical alloying consists of the intimate mixing and mechanical working of the elemental powders in a high-energy ball mill. Compared to the preparation of amorphous alloys by other methods such as rapid cooling, the application of the solid-state amorphization reaction has a number of advantages, including the production of the bulk amorphous materials, composite metal powders, homogeneously alloyed powders and dispersion-strengthened super alloys for jet engine parts, as well as the alloying of the metals with different melting temperatures [7,8]. Amorphous alloys can be formed by milling in two ways: one is to use elemental crystalline powders or amorphous powders and another is to utilize the crystalline alloy [9]. As a result, during the milling there will be a competition between the tendency to go to the thermodynamically stable situation and the tendency to increase the enthalpy due to the energy transferred from the balls to the milling material.

It is the aim of the present paper to survey the preparation of amorphous/nanocrystalline $Ni_{63}Fe_{13}Mo_4Nb_{20}$ magnetic powders by mechanical alloying using elemental crystalline Ni, Fe, Mo and Nb powders. It would be worth mentioning that as compared with the literature in this field, this paper has paid special attention to the amorphization of $Ni_{79}Fe_{16}Mo_5$ commercial alloy by the 20 at% Nb element using the MA method.

The reason for the use of amorphous alloy in the applications of electronics, telecommunications and computers is due to the lower magnetic losses and higher electrical resistivity compared with other magnetic materials.

2. Experimental details

The nickel, iron, molybdenum and niobium powders with the chemical composition of $Ni_{63}Fe_{13}Mo_4Nb_{20}$ in atomic percentage were obtained from Merck with average particle sizes 10, 10, 3 and 3 μm, respectively. Mechanical alloying was carried out in a planetary ball mill on the powders loaded in the vial under argon at a running speed of 350 rpm, together with a blend of steel balls (φ = 10 mm, mass = 4.11 g and φ = 20 mm, mass = 32.60 g) and with a ball to powder weight ratio of 15:1. Prior to milling, about 0.2 wt% of ethanol was added to the powders as a process control agent (PCA). The rotational direction of the instrument changed counterclockwise/clockwise after each 1 h to increase the efficiency. The particles

* Corresponding author. Tel.: +98 917 7016795; fax: +98 711 7354520.
E-mail address: leilakarimi@iauahvaz.ac.ir (L. Karimi).

0925-8388/$ – see front matter © 2011 Elsevier B.V. All rights reserved.
doi:10.1016/j.jallcom.2011.03.060

morphology was studied by scanning electron microscopy (Cam Scan MV2300) and microstructural properties were evaluated by XRD (Shimatzu x2) using Cu Kα in the 2θ range from 30° to 100°. The crystallite size and lattice strain were estimated using the Williamson–Hall method [10]:

$$B\cos\ \theta = 2\varepsilon\ \sin\theta + 0.94\frac{\lambda}{d} \quad (1)$$

where B is the peak integral width, θ is the Bragg angle, d is the grain size, ε is the lattice distortion, and λ is the X-ray wave length. The peak positions in the XRD patterns were determined using three near angle width by fitting the peaks to the Fityk software and the error bars were determined based on three different measurements. The broadening factors that are not induced by MA were taken out by the following equation [10]:

$$B^2 = B_M^2 - B_S^2 \quad (2)$$

where B_S and B_M are the peak integral widths of the initial and the as-received powders, respectively. The lattice parameter of the solid solution alloys was calculated from the XRD patterns using Bragg's law. The amount of amorphous phase was calculated from the internal standard method based on the diffraction pattern from the composite sample. In other words, a diffraction line from the amorphous phase is compared with a line from the standard substance i.e. the tungsten powder which is mixed with the sample and has known proportions [11].

The as-milled powders for TEM characterization were immersed into pure ethanol and dispersed using an ultrasonic vibrator for about 5 min. 200 mesh copper formvar/carbon grids were then used to hold the dispersed powders. A small amount of dispersed powder is dropped on a modified grid using PEI as glue in order not to remove the powder particles in the next two times washing with pure ethanol. The powders were examined using a JEOL 2010 at 200 kV.

The saturation magnetization (M_S), coercive field (H_C) and hysteresis loss were measured as a function of the applied magnetic field in a vibrating sample magnetometer at room temperature between 0 and 10 kOe and the instrumental error is equal to 2%.

3. Results and discussion

3.1. Morphology study

Continuous deformation, cold welding and re-welding occur during the milling. Fig. 1 exhibits the morphological evolution of mixed powder as a function of milling time (0, 8, 48, 96, 120 h). From this figure, it is obvious that different morphologies are present. After 8 h of milling time, the powders flattened with a layered structure due to the introduction of the compressive forces into the particles generated by the ball–powder–ball collisions (Fig. 1b). As a result of intensive fracture and cold welding, composite particles

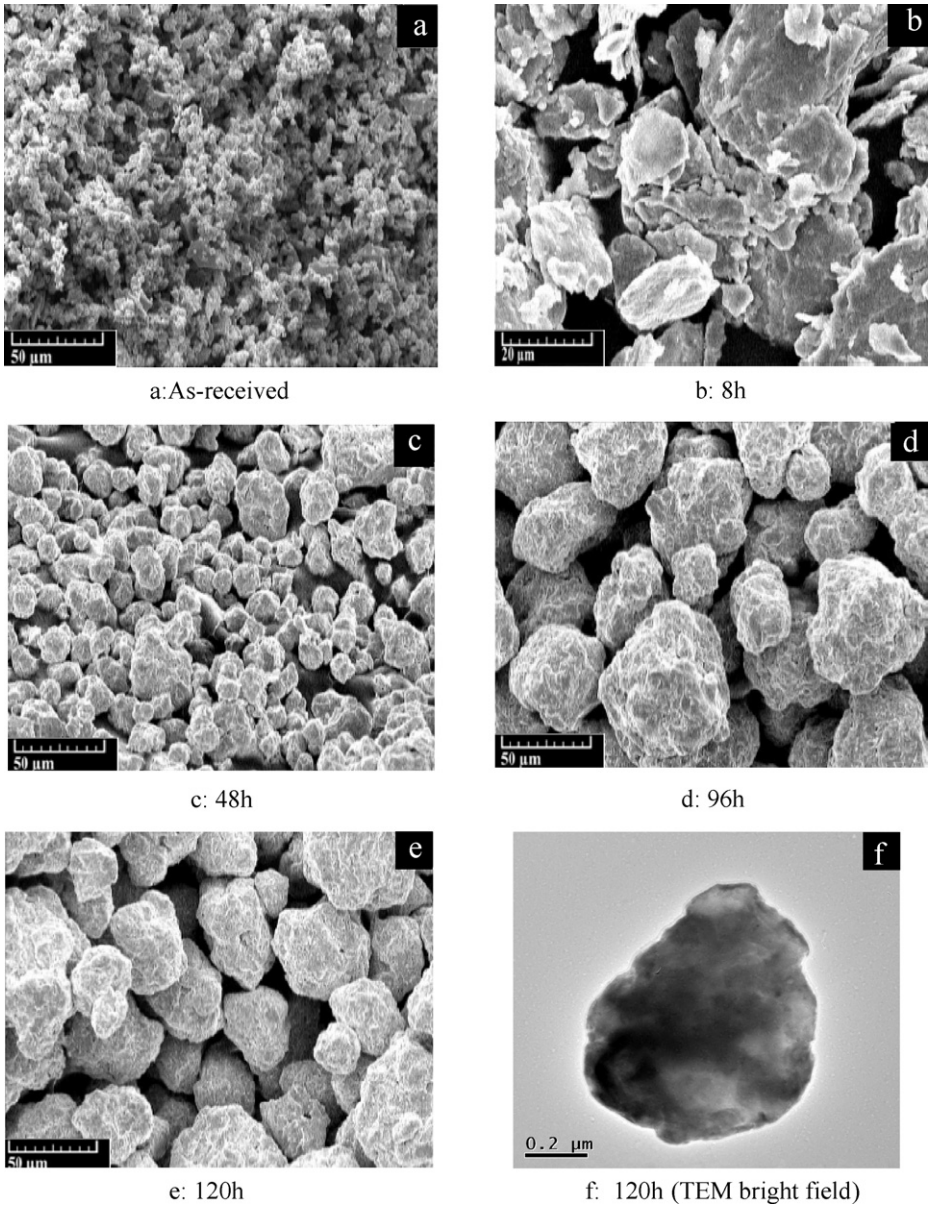

Fig. 1. SEM micrographs of mixed and alloyed powders at different milling times.

were formed after 48 h of milling. The prolonged milling results in a narrower distribution of particle sizes when a balance between the fractures and welding processes is maintained [10] (Fig. 1d and e). In other words, the agglomerated powders are near-spherical ones with high specific and smooth surfaces without any layered-structure morphology. This morphology with the disappearance of the contrast feature can be the characteristic of a typical amorphous powder synthesized by MA [12,13]. Fig. 1f shows the TEM observation bright field of the particle with an average diameter around 1 μm.

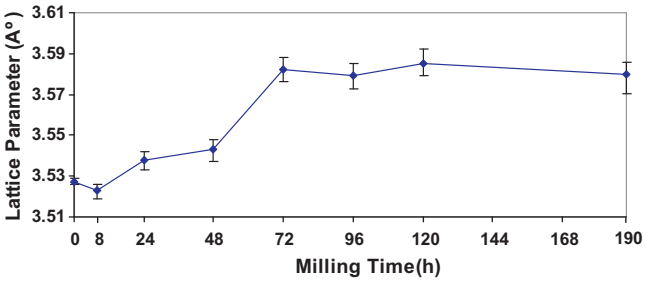

Fig. 3. Lattice parameter vs. milling time.

3.2. XRD observation

3.2.1. Phase identification

Fig. 2 shows a sequence of the XRD patterns regarding the Fe, Ni, Mo and Nb powder mixture milled for various times. The evolution of the X-ray diffraction patterns shows that the mechanical alloying process occurs at three steps:

(a) First, up to 48 h of milling, there is a coexistence of the elemental Fe, Mo, Nb and Ni in the X-ray diffraction patterns. From the XRD spectrum, as the milling time increases, the Fe and Nb lines vanish completely, the Mo main line disappears partially and the Ni peaks shift to the lower 2θ angle and the main Ni peak broaden due to the reduction of the particle size and introduction of lattice strain [10]. These results indicate the formation of the fcc Ni (Fe, Nb, Mo) solid solution due to the complete diffusion of Fe, Nb and partially diffusion of Mo into the Ni lattice.
(b) Second, after 48 h, a broad scattering peak with a small amount of Mo crystalline phase and a peak position shifting observed, indicating the start of the glassy phase formation. As the milling time increases, the amorphous structure and glassy phase become visible up to120 h of milling.
(c) Third, for longer milling time, 190 h, the single broad peak becomes sharper and the small Mo peak disappears. On the other hand, a sharp crystalline peak superimposed to the main halo is observed, implying that the powders have a partially amorphous structure. The observed behavior relates to the mechanical and thermal crystallization of amorphous alloys due to the local pressure and local temperature [14,15], respectively.

3.2.2. Lattice parameter

The plot of the lattice parameter vs. the milling time (Fig. 3) indicates that the lattice parameter decreases and then increases with milling time as diffusion progresses until the maximal allowable solute is consumed to form the solid solution. At first, the lattice parameters decrease when the milling time increases. The reason may be due to the high energy transferred in the collisions allowing for shortening the distance between the atoms in the solid [16], and/or as a result of poor oxidation phenomena at the new particle surfaces formed by comminution during the milling and subsequent trapping of the small quantity of oxygen in the vial [17].

Generally, an increase in the lattice parameter has been found, leading to the solid solution or the amorphous phase formation [18]. From the view point of solution, the atomic radii of the solute atoms of iron, molybdenum and niobium (R_{Fe} = 0.126 nm, R_{Mo} = 0.139 nm, R_{Nb} = 0.146 nm) are larger than that of the nickel (R_{Ni} = 0.124 nm). The value of the lattice parameter increases from 0.352 to 0.358 nm as the milling time increases from 8 to 72 h and then remains constant between 72 and 120 h when the steady-state conditions of milling have been provided and amorphization is completed. Further milling up to 190 h, a slight decrease of lattice parameter is obtained as a result of the partial crystallization from the amorphous state.

3.2.3. Crystallite size

During the milling the mean crystallite size is calculated from the Ni {1 1 1} reflection (Fig. 4), decreases rapidly to an equilibrium value of about 2.5 nm, then remains approximately constant

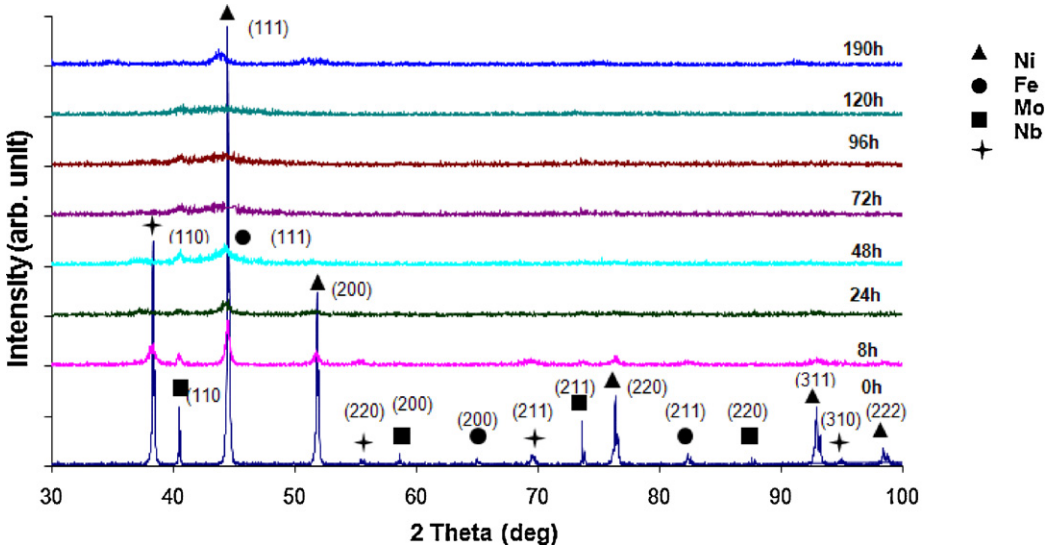

Fig. 2. XRD patterns of as-received and milled powders vs. milling time.

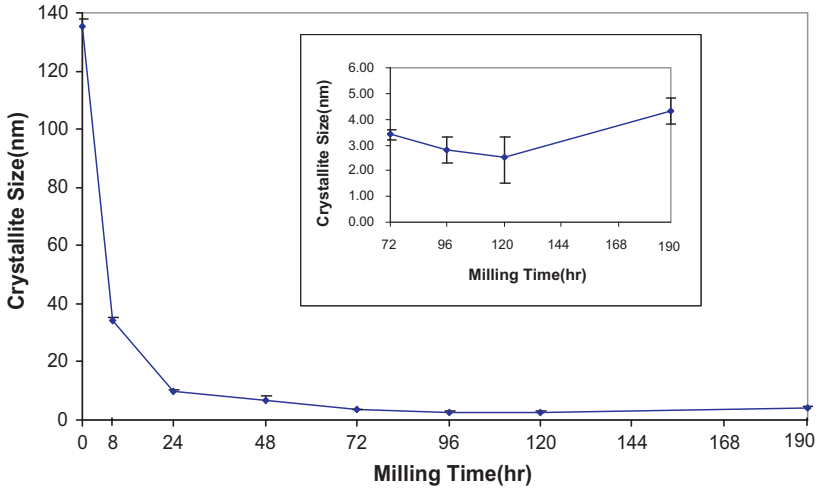

Fig. 4. Average crystallite size vs. milling time.

up to 120 h corresponding to the width of the diffraction peak of the obtained amorphous alloy and finally increases slightly because of the partial crystallization from the amorphous phase.

It should be mentioned that that for severely deformed materials, the average crystallite size determined by XRD analysis is usually lower than the grain size observed in TEM [19]. The grains in severely deformed materials contain sub-grains or dislocation cells which are separated by low-angle grain boundaries. The crystallite size obtained from XRD is equal to the average size of domains which scatter X-rays coherently. As a result, XRD makes a difference between sub-grains or dislocation cells even if the misorientations are very small [19].

As the milling time increases, the volume fraction of grain boundaries led to the domination of the amorphous character and the increase of the grain boundary fraction. The grain boundary fraction is in inverse proportion to grain size and can be written as [20,21]:

$$f_{gb} = \frac{1 - 3d(D-d)^2}{D^3} \quad (3)$$

where d is the effective grain boundary and is approximately 2–3 atomic layers.

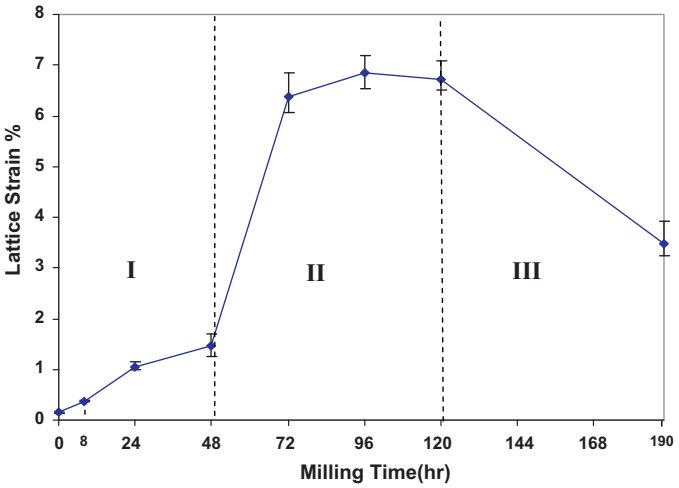

Fig. 5. Variation of lattice strain as a function of milling time.

3.2.4. Micro-strain

Fig. 5 depicts the variation of lattice strain as a function of milling time. From this figure, the three regions can be discussed. Region I: the increase in lattice strain has a microstructure source and is due to the size mismatch between the constituents. Region II: the increase in the lattice strain relates to the increasing the grain boundary fraction, mechanical deformation and dislocation density as a result of severe plastic deformation [22]. Because the bonding in amorphous alloys is of primarily metallic character, strain can be readily accommodated at the atomic level through the changes in the neighborhood and the atomic bonds can be broken and reformed on the atomic scale without substantial concern for, e.g. the rigidity of bond angles as in a covalent solid, or the balance of charges as in an ionic solid [23].

Region III: The main reason for decreasing the micro-strain is high defect concentration sub-grain formation, partial crystal formation and temperature rising [22]. Unlike amorphous alloys the crystal dislocations in new crystal allow for changes in the atomic neighborhood at low energies.

3.3. TEM observation

The amorphous structure of the obtained powder is confirmed from the TEM images. Fig. 6 shows the TEM bright field image and the corresponding selected area diffraction (SAD) analysis of the powder that was milled for 96 h. Fig. 6a shows the high resolution TEM image of the milled $Ni_{63}Fe_{13}Mo_4Nb_{20}$ powder showing a predominantly amorphous microstructure with a few isolated nanometer (<5 nm) crystalline grains. This value is consistent with that obtained from the XRD results (Fig. 2). Fig. 6b depicts the SAD pattern of the alloyed powder showing the amorphous as well as nanocrystalline grains with a few bright spots due to some coarse crystalline grains, such as the Mo particle or milling contaminations. It is obvious that the orientation of the crystallites is quite random and the grain size is small as demonstrated by the uniformity of the diffraction rings.

3.4. Glass forming ability

The glass forming ability (GFA) is quantified in terms of the milling time required to form the glassy phase. Three empirical rules that were considered in great detail by Inoue are defined for the bulk amorphous alloy systems, namely, (a) the requirement of three or more elements; (b) the difference in atomic size ratios among the three main constituent elements and (c) the negative

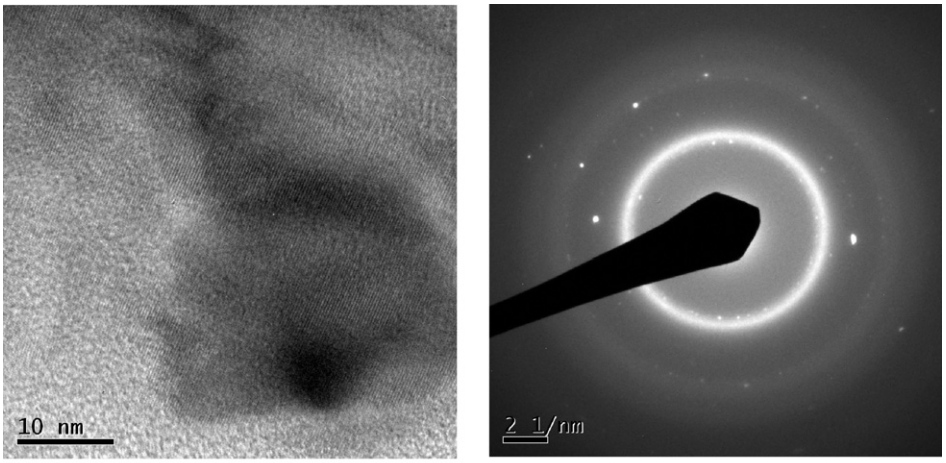

Fig. 6. High resolution image and selected area diffraction at 96 h.

Table 1
Variation of peak position, inter-atomic distance and amorphous content with milling time.

Milling time (h)	0	8	24	48	72	96	120	190
2θ (°)	44.46	44.51	44.30	44.04	43.74	**43.78**	43.71	43.76
d_m (nm)	–	–	–	2.516	2.544	**2.546**	2.545	2.542
Amorphous content (%)	–	–	–	29.0	75.8	**76.8**	75.0	36.5

heats of mixing among the three main constituent elements [7,8]. In other words, the same conditions are true of our experiments as well. Also, the mixing enthalpies have negative ΔH_{mix} (KJ/mol) (Ni–Fe) ~ −5, ΔH_{mix} (KJ/mol) (Ni–Mo) ~ −0.5 and ΔH_{mix} (KJ/mol) (Ni–Nb) ~ −10 [24].

Table 1 lists the variation of the 2θ values, amorphous content and inter-atomic distance (topological/disorder instability) corresponding to the (1 1 1) Ni peak as a function of milling time. During the initial period of milling, the 2θ increases slightly from 8 to 72 the 2θ value corresponding to the (1 1 1) Ni peak decreases, indicating the lattice expansion. This can be related to the formation of the Ni-base solid solution and the dissolution of all the larger metallic elements, including Nb, Fe and Mo substitutionally. However, on continued milling, the 2θ value corresponding to the diffuse peak shifts to higher values, suggesting that a slight lattice contraction has occurred during glass formation. The period of time of 96 h relates to the maximum of the amorphous phase [25].

It is known that the diffraction angle for the first maximum in the XRD spectrum as an instability factor is related to the largest inter-atomic distance [25]. Using the relationship $1.23\lambda = 2d_m \sin\theta$ [25,13,26] (where λ is the wavelength of the X-radiation used, d_m is the distance between the neighboring atoms, θ is the peak position and 1.23 is the correction factor used for liquid and amorphous solids), it is possible to determine the distance between the nearest-neighbor atoms from the θ values observed. The value of d_m or instability factor means the volumetric strain or topological instability.

3.5. Magnetic studies

Fig. 7 illustrates the hysteresis loop and magnetization curve of $Ni_{63}Fe_{13}Mo_4Nb_{20}$ powders at different milling times and room temperature. From this figure, it is obvious that the hysteresis loop distorts under mechanical stress. The increase in magnetization and magnetic susceptibility up to 8 h confirms the solubility Fe ($2.2\mu_B$) in the Ni ($0.6\mu_B$) lattice [27]. The decrease of magnetization and magnetic susceptibility of the milled powder for 72 and 120 h reveals a high disorder/defect structure, a relatively large inter-atomic distance between magnetic atoms and the presence of the Nb paramagnetic atom. These variations are accompanied by an increase in saturation magnetization and magnetic susceptibility

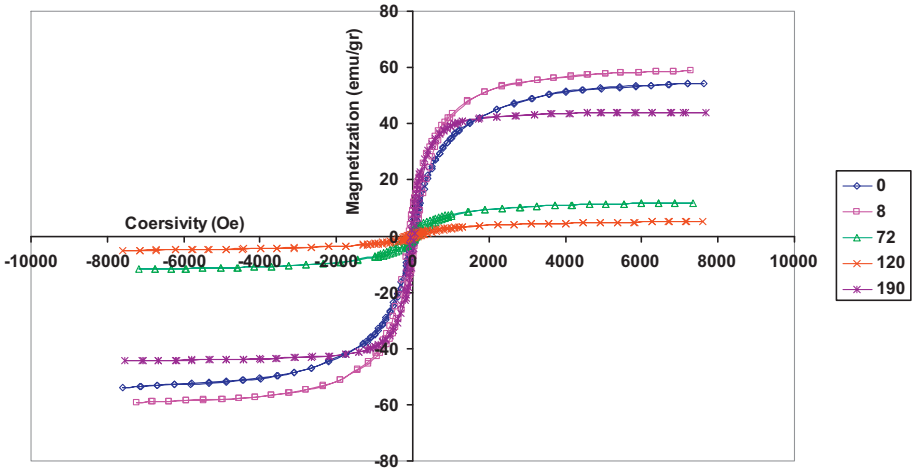

Fig. 7. Hysteresis loops of different milled powders at room temperature.

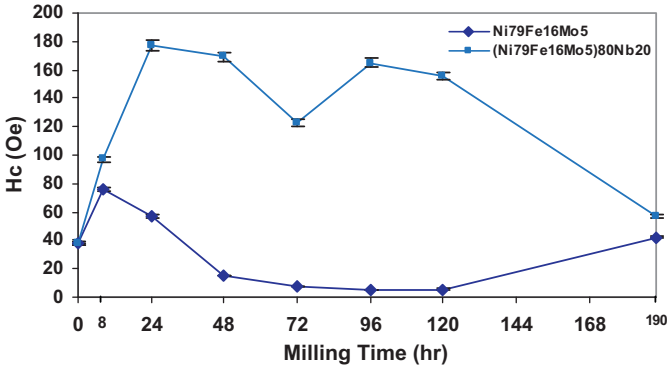

Fig. 8. Magnetic coercivity as a function of milling time for two different compositions at room temperature.

as a result of a reduction in micro-strain and a small crystallization from the amorphous matrix.

3.5.1. Coercivity

Magnetic coercivity is highly structural-sensitive and strongly depends on the real structure of the material, but its intrinsic part depends on magnetic anisotropy. Fig. 8 illustrates the variation of the H_C with milling time. At the early stages up to 24 h, the extrinsic parameters including micro-strain and especially grain size are dominant ($H_C \propto d^{-1}$) and act as pinning sites, consequently the magnetic coercivity increases. Over a period of 24 h the grain size approaches the critical value (~15 nm), causing the Herzer model to act [10] and consequently the coercivity maximizes. At milling times between 24 and 72 h, the grain size decreases noticeably from 10 to 3 nm. In this region, below the critical grain size, the coercivity theoretically relates to the grain size by a power ~6 ($H_C \propto d^6$), consequently H_C decreases. After 72 h, the grain size remains approximately in a constant level. In this region the micro-strain is a dominant factor and leads to an increases in coercivity (Eq. (4)). Micro-strain can be related to the H_C by the following linear equation [27]:

$$H_C \propto \frac{\lambda_s \Delta_s \delta_w}{\mu_0 M_s} \quad (4)$$

where δ_w is the wall thickness, λ_s is the magnetostriction coefficient, and $\Delta\sigma$ is the internal stress. With increasing the milling time between 120 and 190 h the magnetic coercivity decreases and this behavior can be expressed by the following points:

a. The noticeable decrease in micro-strain as illustrated in Fig. 5.
b. The increase in M_S leads to a reduction in H_C based on the following formula [28].

$$H_C \approx 3\gamma_w / J_s d \quad (5)$$

where J_s is the saturation polarization, γ_w is the wall energy, which is proportional to $(K_1)^{1/2}$, and K_1 is the first order magnetocrystalline anisotropy constant.
c. The complete solution of Mo results in decreasing the long-range ordering [29] and then leads to the reduction in magnetic anisotropy.

From Fig. 8, the effect of Nb content on the coercivity can be followed. It is clear that, the sample with 20% Nb has a higher coercivity level in comparison with the other samples. The difference in magnetic behavior relates to the higher stresses and defects as a result of amorphization and the nature of Nb element. For the alloy containing Nb the tendency is to the increase of the strength of interaction between the unfilled 3d (Ni, Fe) and 4d (Nb) electronic shells and magnetocrystalline anisotropy [27].

3.5.2. Magnetization saturation

Saturation magnetization is the property which refers to the atomic origin of magnetism. It strongly depends on the chemical composition of the local environment of atoms and their electronic structure in bulk materials. It involves quantum phenomena, such as exchange, crystal-field interaction, inter-atomic hopping and spin-orbit coupling [26]. Fig. 9 displays the variation of saturation magnetization with milling time for two different compositions. For more effective discussions, this graph has been divided into three regions.

Region I: The M_S increases slightly at the early stage up to 8 h. The moment of Ni–Fe based alloys originates from nearly exclusively the partly filled 3d inner electron shells. At early stages, the Fe ($2.2\mu_B$) atoms are solved into Ni ($0.6\mu_B$) lattice and increase the M_S. From the band theory of ferromagnetism, the density of the states in the 3d shell of Ni may be very high at the top of the 3d ban [26,27]. Fe atoms ($[Ar]4s^2 3d^6$) have two more vacancies in the 3d shell than the Ni atoms (Ni: $[Ar]4s^2 3d^8$) in the matrix. Therefore, it seems that an iron atom in the matrix should have two more Bohr magnetons than the Ni atom.

Region II: From 8 to 120 h, M_S decreases with milling time. This falling can be attributed to the solution of Nb ($[Kr]5s^1 4d^4$) and Mo ($[Kr]5s^1 4d^5$) in the lattice. The addition of non-ferromagnetic elements of Mo and Nb decreases the proportion of nickel magnetic atoms, thereby reducing the density of the magnetic atom interactions [26]. This reduction leads to the lower exchange interaction between Ni atoms and Ni–Fe and the suppression of the Ni metal moment by the charge transfer to the d-band and by the d–d hybridization which decreases the number of polarization d states. Furthermore, the presence of the Mo element slows down the ordering kinetics and lowers slightly the magnetization [28,29]. The strength of the d-electron bonding increases from 3d to 4d [30,31], indicating that the stability of the pair bonds between Ni–Nb and Mo should be higher than the iron series.

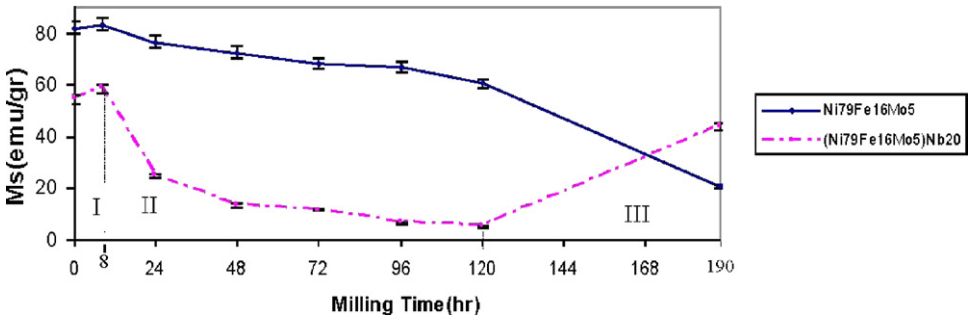

Fig. 9. Saturation magnetization as a function of milling time for two different compositions at room temperature.

Region III: From 120 up to 190 h, saturation magnetization increases due to the partial crystallization (Fig. 2) and as a result of a decrease in the inter-atomic distance between magnetic atoms (Table 1).

4. Conclusions

It is well known that both the magnetic and structural properties of the metallic materials are influenced by crystal defects including grain boundaries, solute atoms and dislocations. The mechanical alloying of Ni, Fe, Mo and Nb powders was investigated. The process leads to the alloying of the element powders, the nanocrystalline and an amorphization matrix with Mo element up to 120 h accompanied by the strain and thermal-induced nucleation of a single nanocrystalline Ni-based phase from amorphous matrix at 190 h. The results revealed that the coercive force increases due to the strain-defect induction and complete solution of Nb. At last the coercive force decreases due to the complete solution of Mo and a reduction in micro-strain. In addition, the saturation magnetization decreases as a result of the electronic interactions between magnetic and nonmagnetic elements and finally increases by the partial crystallization of the amorphous matrix.

Acknowledgements

The authors wish to thank Shiraz University of Technology for providing the related investigators with Powder Processing Lab Equipment and Islamic Azad University of Ahvaz for partial financial support. Also, the authors wish to thank Prof. K. Janghorban for helpful discussions.

References

[1] V. Hays, R. Marchand, G. Saindrenan, E. Gaffet, Nanostruct. Mater. 7 (1996) 411–420.
[2] M. Pekala, D. Oleszak, E. Jartych, J.K. Zurawicz, Nanostruct. Mater. 11 (1999) 789–796.
[3] H. Shokrollahi, Materials 30 (2009) 3374–3387.
[4] H. Shokrollahi, R. Koohkan, Sh. Sharafi, K. Janghorban, J. Magn. Magn. Mater. 320 (2008) 1089–1094.
[5] J. Fuzer, P. Kollar, D. Oleksakova, S. Roth, J. Alloys Compd. 483 (2009) 557–559.
[6] R. Hasegawa, J. Non-Cryst. Solids 287 (2001) 405–412.
[7] R. Hasegawa, Mater. Sci. Eng., A 375–377 (2004) 90–97.
[8] H. Chiriac, N. Lupu, Mater. Sci. Eng., A 375–377 (2004) 255–259.
[9] A.W. Weeber, H. Bakker, Physica B 153 (1988) 93–135.
[10] H. Shokrollahi, M. Delshad Chermahini, M. Zandrahimi, Sh. Sharafi, Alloys Compd. 477 (2009) 45–50.
[11] B.D. Cullity, Elements of X-ray Diffraction, Second ed., Addison-Wesley Publishing Company Inc., 1978.
[12] M.S. El-Eskandarany, A.A. Bahgat, N.S. Gomaa, N.A. Eissa, J. Alloys Compd. 290 (1999) 181–190.
[13] L. Liu, J. Zhang, Mater. Res. Bull. 36 (2001) 2073–2082.
[14] J. Xu, M. Atzmon, Appl. Phys. Lett. 73 (1998) 1805–1809.
[15] L. Liu, S. Lun, S.E. Liu, X.D. Zhao, B. Yao, W.H. Su, J. Alloys Compd. 333 (2002) 202–206.
[16] D.C. Palacio, J.F. Vallderruten, L.E. Zamora, P. Alcázar, J.A. Tabares, Hyperfine Interact. 195 (2010) 241–245.
[17] G. Principi, T. Spataru, A. Maddalena, S. Gialanella, Hyperfine Interact. 139/140 (2002) 315–318.
[18] R. Hamzaoui, O. Elkedim, N. Fenineche, E. Gaffet, J. Craven, Mater. Sci. Eng., A 360 (2003) 299–305.
[19] A. Sarkar, A. Bhowmik, S. Suwas, Appl. Phys. A 94 (2009) 943–948.
[20] C. Suryanarayana, Mechanical Alloying and Milling, Marcel Dekker, New York, 2004.
[21] J.M. Greneche, A.J. Slawska-Waniewska, Magn. Magn. Mater. 215–214 (2000) 264–267.
[22] Y. Shen, H. Hoon Hng, J. Tien, J. Alloys Compd. 379 (2004) 266–271.
[23] A.S. Christopher, C.H. Todd, Acta Mater. 55 (2007) 4067–4109.
[24] C.L. Yaws, Handbook of Thermodynamic Diagrams, Volume 4: Inorganic Compounds and Elements, vol. 4, Gulf Publishing Company, 1996.
[25] S. Sharma, C. Suryanarayana, Scr. Mater. 58 (2008) 508–511.
[26] D.B. Miracle, W.S. Sanders, Philos. Mag. 83 (2003) 2409–2428.
[27] R.L. Comstock, Introduction to Magnetism and Magnetic Recording, Wiley, NewYork, 1999.
[28] K. Gupta, K.K. Raina, S.K. Sinha, J. Alloys Compd. 429 (2007) 357–364.
[29] D. Oleksˇaïkovaï, P. Kollaïr, J. Fu¨zer, M. Kusyï, S. Roth, K. Polanski, J. Magn. Magn. Mater. 316 (2007) e838–842.
[30] H. Wu, S.R. Desai, L.-S. Wang, Phys. Rev. Lett. 76 (1996) 212–220.
[31] J.B. Staunton, S.S.A. Razee, M.F. Ling, D.D. Johnson, F.J. Pinski, J. Phys. D: Appl. Phys. 31 (1998) 2355–2367.